

DREAM: Diffusion Rectification and Estimation-Adaptive Models

Jinxin Zhou^{1*}Tianyu Ding^{2*†}Tianyi Chen²Jiachen Jiang¹Ilya Zharkov²Zhihui Zhu¹Luming Liang^{2†}¹Ohio State University²Microsoft

{zhou.3820, jiang.2880, zhu.3440}@osu.edu, {tianyuding, tiachen, zharkov, lulian}@microsoft.com

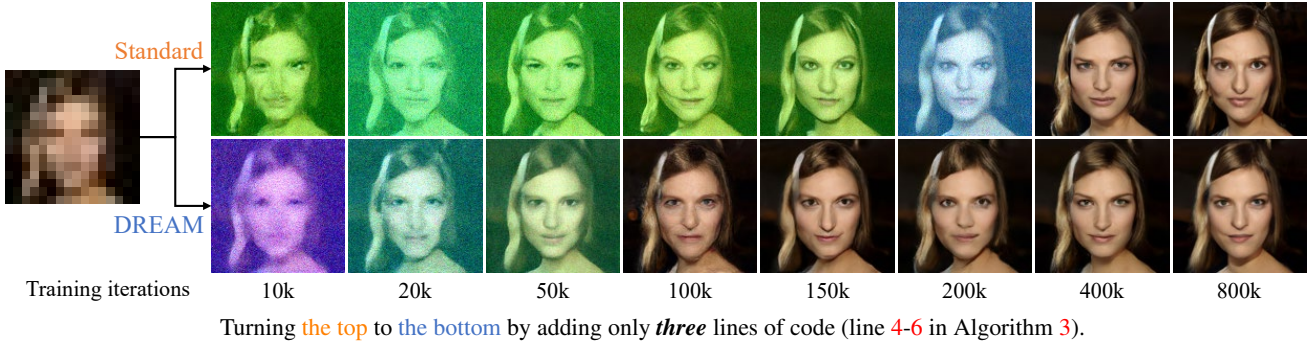


Figure 1. Comparative training of conditional diffusion models for super-resolution. Top: standard conditional DDPM [44]. Bottom: enhancing the same model training with just *three* additional lines of code, leaving the sampling process unchanged. DREAM facilitates notably faster and more stable training convergence, significantly surpassing baseline models in key metrics of perception and distortion.

Abstract

We present **DREAM**, a novel training framework representing **Diffusion Rectification and Estimation-Adaptive Models**, requiring minimal code changes (just *three* lines) yet significantly enhancing the alignment of training with sampling in diffusion models. DREAM features two components: diffusion rectification, which adjusts training to reflect the sampling process, and estimation adaptation, which balances perception against distortion. When applied to image super-resolution (SR), DREAM adeptly navigates the tradeoff between minimizing distortion and preserving high image quality. Experiments demonstrate DREAM’s superiority over standard diffusion-based SR methods, showing a 2 to 3× faster training convergence and a 10 to 20× reduction in necessary sampling steps to achieve comparable or superior results. We hope DREAM will inspire a rethinking of diffusion model training paradigms. [\[Project page\]](#)

1. Introduction

Single-image super-resolution (SISR) [3, 12, 50, 59] involves generating high-resolution (HR) images from low-

resolution (LR) counterparts, a process crucial in various applications including video surveillance, medical diagnosis, and photography. SISR is challenging due to the diverse real-world degradation patterns and the inherent ill-posed nature of the task, where different HR images can correspond to the same LR image.

SISR methods are generally categorized into regression-based and generation-based approaches. Regression-based methods [7, 31, 34, 69] focus on minimizing pixel-level discrepancies, *i.e.*, distortion, between SR predictions and HR references. However, this approach often fails to capture the perceptual quality of images. To address this, generation-based methods employ deep generative models, including autoregressive models [40, 41], variational autoencoders (VAEs) [27, 53], normalizing flows (NFs) [11, 26], and generative adversarial networks (GANs) [16, 24, 33, 42], aiming to improve the perceptual aspects of SR images.

Recently, Diffusion Probabilistic Models (DPMs) [19, 48], a novel class of generative models, have attracted increased interest for their impressive generative abilities, especially in the SISR task [14, 20, 43, 44, 62]. Nonetheless, DPM-based methods face challenges due to their dependence on a long sampling chain, which can lead to error accumulation and reduce training and sampling efficiency. A further issue is the discrepancy between training and sam-

*Equal contribution. †Corresponding author.

pling [39, 61]: training typically involves denoising noisy images conditioned on ground truth samples, whereas testing (or sampling) conditions on previously self-generated results. This disparity, inherent in the multi-step sampling process, tends to magnify with each step, thereby constraining the full potential of DPMs in practice.

To bridge the gap between training and sampling in diffusion models, we introduce DREAM, an end-to-end training framework denoting Diffusion Rectification and Estimation-Adaptive Models. DREAM consists of two key elements: *diffusion rectification* and *estimation adaptation*. Diffusion rectification extends traditional diffusion training with an extra forward pass, enabling the model to utilize its own predictions. This approach accounts for the discrepancy between training (using ground-truth data) and sampling (using model-generated estimates). However, solely relying on this self-alignment can compromise perceptual quality for the sake of reducing distortion. To counter this, our estimation adaptation strategy balances standard diffusion and diffusion rectification by adaptively incorporating ground-truth information. This approach smoothly transitions focus between the two by adaptively injecting ground-truth information. This integration harmonizes the advantages of both approaches, effectively reducing the training-sampling discrepancy, as demonstrated in Figure 3.

The DREAM framework excels in its simplicity, easily integrating into existing diffusion-based models with only three lines of code and requiring no alterations to the network architecture or sampling process. When applied to the SR task, DREAM has notably improved generation quality across various diffusion-based SR methods and datasets. For example, on the $8\times$ CeleA-HQ dataset, it boosts the SR3 [44] method’s PSNR from 23.85 dB to 24.63 dB while reducing the FID score from 61.98 to 56.01. Additionally, DREAM accelerates training convergence by 2 to 3 times and improves sampling efficiency, requiring 10 to 20 times fewer steps for comparable or superior results. It also demonstrates enhanced out-of-distribution (OOD) SR results compared to baseline methods.

Our contributions are summarized as follows:

- We introduce DREAM, a simple yet effective framework to alleviate the training-sampling discrepancy in standard diffusion models, requiring minimal code modifications.
- We demonstrate the application of DREAM to various diffusion-based SR methods, resulting in significant improvements in distortion and perception metrics.
- The proposed DREAM also notably speeds up training convergence, enhances sampling efficiency, and delivers superior out-of-distribution (OOD) results.

2. Related work

Super-resolution. In single-image super-resolution, substantial efforts [2, 9, 10, 15, 22, 28, 33, 47, 63, 64, 68, 69]

have been devoted to two primary categories: regression-based and generation-based. Regression-based methods, such as EDSR [34], RRDB [57], and SWinIR [31], focus on a direct mapping from LR to HR images, employing pixel-wise loss to minimize differences between SR images and their HR references. While effective in reducing distortion, these methods often yield overly smooth, blurry images. Generation-based methods, on the other hand, aim to produce more realistic SR images. GAN-based models, like SRGAN [28], combine adversarial and perceptual losses [65] to enhance visual quality. Methods of this line include SFTGAN [56] and GLEAN [5], which integrate semantic information to improve texture realism. ESRGAN [57] further refines SRGAN’s architecture and loss function. However, GAN-based methods often face challenges like complex regularization and optimization to avoid instability. Autoregressive models (e.g., Pixel-CNN [54], Pixel-RNN [41], VQVAE [55], and LAR-SR [17]) are computationally intensive and less practical for HR image generation. Normalizing Flows (NFs) [11, 26] and VAEs [27, 53] also contribute to the field, but these methods sometimes struggle to produce satisfactory results.

Diffusion model. Inspired by non-equilibrium statistical physics, [48] first proposes Diffusion Probabilistic Models (DPMs) to learn complex distributions. These models have since advanced significantly [8, 19, 37, 49], achieving state-of-the-art results in image synthesis. Beyond general image generation, diffusion models have shown remarkable utility in low-level vision tasks, particularly in SR. Notable examples include SR3 [44], which excels in image super-resolution through iterative refinement, and IDM [14], which blends DPMs with explicit image representations to enable flexible generation across various resolutions. SRDiff [29] uniquely focuses on learning the residual distribution between HR and LR images through diffusion processes. LDM [43] deviates from traditional pixel space approaches, employing cross-attention conditioning for diffusion in latent space. Building upon LDM, ResShift [62] employs a refined transition kernel for sequentially transitioning the residual from LR embeddings to their HR counterparts.

Training-sampling discrepancy. [39] first analyzes the training-sampling discrepancy in unconditional diffusion models, proposing to represent estimation errors with a Gaussian distribution for improved DPM training. This discrepancy was later attributed by [61] to a constant training weight strategy, suggesting a reweighted objective function based on the signal-to-noise ratio at different diffusion steps. In addition, [30] adjusts the distribution during the sampling process by choosing the optimal step within a pre-defined windows for denoising at each stage. [38] applies a predefined linear function to adjust noise variance during sampling, and [13] recommends starting the sampling from

Algorithm 1 Conditional DDPM Training

```

1: repeat
2:    $(\mathbf{x}_0, \mathbf{y}_0) \sim p(\mathbf{x}_0, \mathbf{y}_0), t \sim \mathbb{U}(1, T), \boldsymbol{\epsilon}_t \sim \mathcal{N}(\mathbf{0}, \mathbf{I})$ 
3:   Compute  $\mathbf{y}_t = \sqrt{\bar{\alpha}_t} \mathbf{y}_0 + \sqrt{1 - \bar{\alpha}_t} \boldsymbol{\epsilon}_t$ 
4:   Update  $\theta$  with gradient  $\nabla_{\theta} \|\boldsymbol{\epsilon}_t - \boldsymbol{\epsilon}_{\theta}(\mathbf{x}_0, \mathbf{y}_t, t)\|_1$ 
5: until converged

```

an approximate distribution that mirrors the training process in terms of frequency and pixel space.

Our approach, distinct from previous unconditional methods, addresses discrepancies based on predictions relative to the conditional input data, ensuring a tailored and accurate solution for complex visual prediction tasks like SISR. Our method also draws inspiration from step-unrolling techniques in depth estimation [21, 46] and text generation [45], leveraging the model's own predictions for error estimation. However, we uniquely integrate self-estimation with adaptive incorporation of ground-truth data. This integration, guided by the pattern of estimation errors, effectively balances perceptual quality and distortion, enhancing generated image qualities.

3. Method

3.1. Preliminaries

The goal of SR is to recover a high-resolution (HR) image from its low-resolution (LR) counterpart. This task is recognized as ill-posed due to its one-to-many nature [44, 62], and is further complicated by various degradation models in real-world scenarios. Notably, diffusion models [19, 48] have emerged as powerful generative models, showcasing strong capabilities in image generation tasks. Following [44], we address the SR challenge by adapting a *conditional* denoising diffusion probabilistic (DDPM) model. This adaptation, conditioned on the LR image, sets it apart from traditional, unconditional models which are primarily designed for unconstrained image generation.

We denote the LR and HR image pair as $(\mathbf{x}_0, \mathbf{y}_0)$. A conditional DDPM model involves a Markov chain, encompassing a *forward process* that traverses the chain, adding noise to \mathbf{y}_0 , and a *reverse process*, which conducts reverse sampling from the chain for denoising from pure Gaussian noise to the HR image \mathbf{y}_0 , conditioned on the LR image \mathbf{x}_0 .

Forward process. The forward process, also referred to as the diffusion process, takes a sample \mathbf{y}_0 and simulates the non-equilibrium thermodynamic diffusion process [48]. It gradually adds Gaussian noise to \mathbf{y}_0 via a fixed Markov chain of length T :

$$q(\mathbf{y}_t | \mathbf{y}_{t-1}) = \mathcal{N}(\mathbf{y}_t; \sqrt{1 - \beta_t} \mathbf{y}_{t-1}, \beta_t \mathbf{I}), \quad (1)$$

$$q(\mathbf{y}_{1:T} | \mathbf{y}_0) = \prod_{t=1}^T q(\mathbf{y}_t | \mathbf{y}_{t-1}), \quad (2)$$

Algorithm 2 Conditional DDPM Sampling

```

1:  $\mathbf{y}_T \sim \mathcal{N}(\mathbf{0}, \mathbf{I})$ 
2: for  $t = T \cdots 1$  do
3:    $\mathbf{z} \sim \mathcal{N}(\mathbf{0}, \mathbf{I})$  if  $t > 1$  else  $\mathbf{z} = \mathbf{0}$ 
4:    $\mathbf{y}_{t-1} = \frac{1}{\sqrt{\bar{\alpha}_t}} (\mathbf{y}_t - \frac{1 - \alpha_t}{\sqrt{1 - \bar{\alpha}_t}} \boldsymbol{\epsilon}_{\theta}(\mathbf{x}_0, \mathbf{y}_t, t)) + \sigma_t \mathbf{z}$ 
5: end for
6: return  $\mathbf{y}_0$ 

```

where $\{\beta_t \in (0, 1)\}_{t=1}^T$ is the variance scheduler. As the step t increases, the signal \mathbf{y}_0 gradually loses its distinguishable features. Ultimately, as $t \rightarrow \infty$, \mathbf{y}_t converges to an isotropic Gaussian distribution. Moreover, we can derive the distribution for sampling at arbitrary step t from \mathbf{y}_0 :

$$q(\mathbf{y}_t | \mathbf{y}_0) = \mathcal{N}(\mathbf{y}_t; \sqrt{\bar{\alpha}_t} \mathbf{y}_0, (1 - \bar{\alpha}_t) \mathbf{I}). \quad (3)$$

where $\bar{\alpha}_t = \prod_{i=1}^t \alpha_i$ and $\alpha_t = 1 - \beta_t$.

Reverse process. The reverse process, also referred to as the denoising process, learns the conditional distributions $p_{\theta}(\mathbf{y}_{t-1} | \mathbf{y}_t, \mathbf{x}_0)$ for denoising from Gaussian noise to \mathbf{y}_0 conditioned on \mathbf{x}_0 , through a reverse Markovian process:

$$p_{\theta}(\mathbf{y}_{t-1} | \mathbf{y}_t, \mathbf{x}_0) = \mathcal{N}(\mathbf{y}_{t-1}; \boldsymbol{\mu}_{\theta}(\mathbf{x}_0, \mathbf{y}_t, t), \sigma_t^2 \mathbf{I}), \quad (4)$$

$$p_{\theta}(\mathbf{y}_{0:T} | \mathbf{x}_0) = p(\mathbf{y}_T) \prod_{t=1}^T p_{\theta}(\mathbf{y}_{t-1} | \mathbf{y}_t, \mathbf{x}_0), \quad (5)$$

where σ_t is a predetermined term related to β_t [19].

Training. We train a denoising network $\boldsymbol{\epsilon}_{\theta}(\mathbf{x}_0, \mathbf{y}_t, t)$ to predict the noise vector $\boldsymbol{\epsilon}_t$ added at step t . Following [19, 44], the training objective can be expressed as:

$$\mathcal{L}(\theta) = \mathbb{E}_{(\mathbf{x}_0, \mathbf{y}_0), \boldsymbol{\epsilon}_t, t} \|\boldsymbol{\epsilon}_t - \boldsymbol{\epsilon}_{\theta}(\mathbf{x}_0, \mathbf{y}_t, t)\|_1. \quad (6)$$

With Eq. (3), we parameterize $\mathbf{y}_t = \sqrt{\bar{\alpha}_t} \mathbf{y}_0 + \sqrt{1 - \bar{\alpha}_t} \boldsymbol{\epsilon}_t$, and summarize the training process in Algorithm 1.

Sampling. In essence, the training minimizes the divergence between the forward posterior $q(\mathbf{y}_{t-1} | \mathbf{y}_t, \mathbf{y}_0)$ and $p_{\theta}(\mathbf{y}_{t-1} | \mathbf{y}_t, \mathbf{x}_0)$, and the mean $\boldsymbol{\mu}_{\theta}(\mathbf{x}_0, \mathbf{y}_t, t)$ in Eq. (4) is parameterized [44] to match the mean of $q(\mathbf{y}_{t-1} | \mathbf{y}_t, \mathbf{y}_0)$:

$$\boldsymbol{\mu}_{\theta}(\mathbf{x}_0, \mathbf{y}_t, t) = \frac{1}{\sqrt{\bar{\alpha}_t}} (\mathbf{y}_t - \frac{1 - \alpha_t}{\sqrt{1 - \bar{\alpha}_t}} \boldsymbol{\epsilon}_{\theta}(\mathbf{x}_0, \mathbf{y}_t, t)). \quad (7)$$

To sample $\mathbf{y}_0 \sim p_{\theta}(\mathbf{y}_0 | \mathbf{x}_0)$, starting from $\mathbf{y}_T \sim \mathcal{N}(\mathbf{0}, \mathbf{I})$, we reverse the Markovian process by iteratively sampling $\mathbf{y}_{t-1} \sim p(\mathbf{y}_{t-1} | \mathbf{y}_t, \mathbf{x}_0)$ based on Eqs. (4) and (7), which completes the sampling process, as shown in Algorithm 2.

3.2. Challenge: training-sampling discrepancy

Training diffusion models for SR presents a critical challenge, stemming from a discrepancy between the training and inference phases, which we term as *training-sampling discrepancy*. During the training phase, the model operates on actual data, wherein the noisy image \mathbf{y}_t at diffusion step t is derived from the *ground-truth* HR image \mathbf{y}_0 as per line 3 in Algorithm 1. However, during the inference

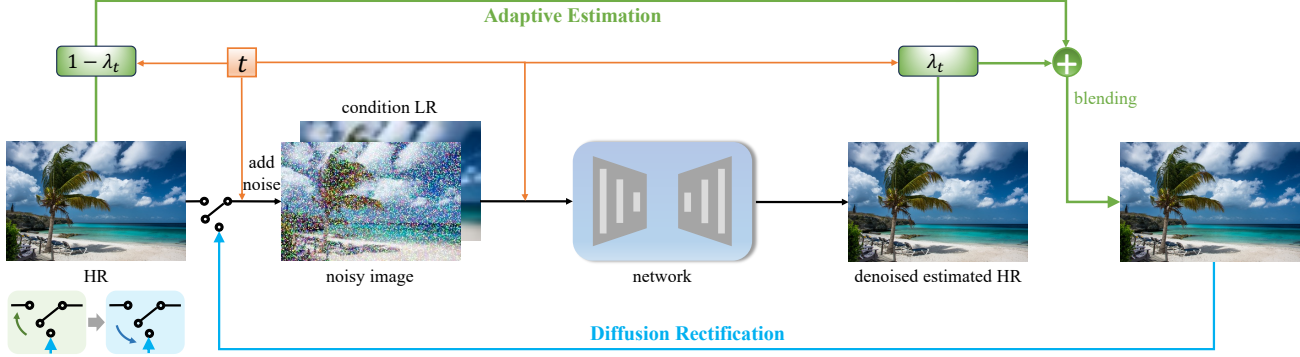


Figure 2. **Overview of the DREAM framework.** Starting with ground-truth HR images, a standard diffusion process with a frozen denoiser network generates denoised HR estimates. The **Adaptive Estimation** merges these estimated HR images with the original HR images, guided by the pattern of estimation errors. The **Diffusion Rectification** constructs the noisy images from this merged HR images, which are then fed into the denoiser network (now unfrozen). Similar to DDPM [19], the denoiser network is trained to eliminate both the introduced Gaussian noise and errors arising from the training-sampling discrepancy, as detailed in Eq. (14).

phase, the ground truth y_0 is unavailable. As outlined in line 4 in Algorithm 2, the model now operates on predicted data, where y_t is obtained from the preceding sampling step $t + 1$. Due to the estimation error, the noisy image y_t constructed in these two processes usually differs, giving rise to the training-sampling discrepancy.

To better illustrate the discrepancy, we conduct an experiment utilizing a pre-trained SR3 model [44], denoted by ϵ_θ , adhering to the standard diffusion training framework. The goal is to understand the implications for HR signal y_0 reconstruction under two distinct scenarios:

- “Training”. Simulating the training process, we *assume access* to the ground-truth y_0 , and construct the noisy image at time step t as per line 3 in Algorithm 1, denoting the image as y_t^{train} .
- “Sampling”. Simulating the sampling process, we *assume no access* to y_0 and iteratively construct the noisy image at each time step t by sampling from the previous step, as per line 4 in Algorithm 2. The noisy image thus obtained is denoted by y_t^{sample} .

To retrieve the HR image y_0 from the noisy image in both scenarios, we utilize Eq. (3) and the pre-trained network ϵ_θ to compute the predicted HR signal as follows:

$$\tilde{y}_0 = \frac{1}{\sqrt{\bar{\alpha}_t}} (y_t - \sqrt{1 - \bar{\alpha}_t} \epsilon_\theta(x_0, y_t, t)) =: h_\theta(y_t). \quad (8)$$

Following this, we compute $\tilde{y}_0^{\text{train}} = h_\theta(y_t^{\text{train}})$ and $\tilde{y}_0^{\text{sample}} = h_\theta(y_t^{\text{sample}})$ as the predicted HR images in the “training” and “sampling” scenarios, respectively. For performance evaluation, we take 100 samples from FFHQ [25] and calculate the averaged MSE and LPIPS [65] metrics between the predicted HR images and the ground-truth y_0 across various time step t under the defined settings.

We present the findings in Figure 3a, where both MSE and LPIPS exhibit a decline with a smaller t , as expected, since the network can reconstruct more accurate HR sig-

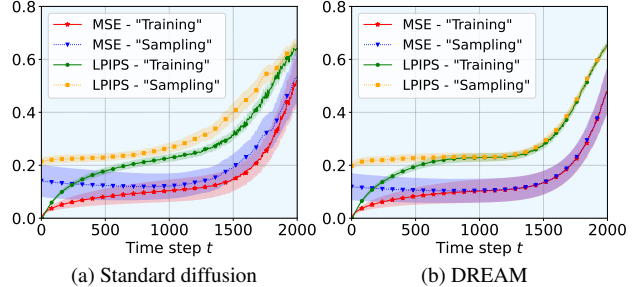


Figure 3. Evaluation of training-sampling discrepancy and its alleviation through our DREAM framework. The mean curve over 100 samples at each time step t is plotted, with the shaded area representing the standard deviation of each metric. Here, $T = 2000$.

nal from less noisy input. Importantly, discernible disparities are observed between the curves representing the “training” and “sampling” settings—the “training” curves consistently exhibit lower error compared to the “sampling” ones, suggesting the advantage of having access to the ground-truth y_0 for improved prediction accuracy. In contrast, Figure 3b illuminates a remarkable alleviation in this discrepancy when employing our DREAM framework to train the identical SR3 architecture: *the “sampling” curve closely aligns with the “training” curve, despite the lack of access to the ground-truth y_0 , across both MSE and LPIPS metrics.* This underscores the efficacy of our approach in bridging the training-sampling discrepancy and thereby facilitating more accurate predictions.

3.3. The DREAM framework

We now present our DREAM framework (see Figure 2), an end-to-end training strategy designed to bridge the gap between training and sampling in diffusion models. It consists of two core components: *diffusion rectification* and *estimation adaptation*, which we elaborate as follows.

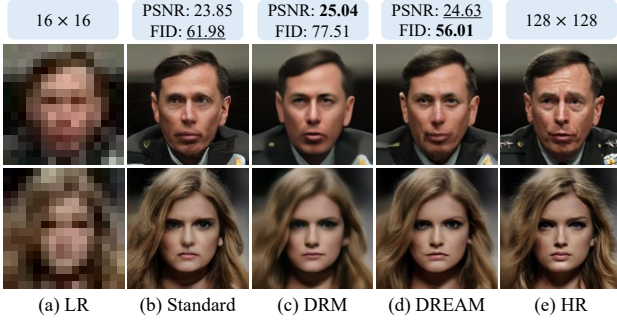


Figure 4. 8× SR on the CelebA-HQ dataset [23].

Diffusion rectification. The goal of diffusion rectification is to modify the behavior of the diffusion training to account for the training-sampling discrepancy, which arises from the manner in which we construct the intermediate signals—either from the ground-truth or from the model’s own estimation. Hence, we extend the diffusion training framework to align more closely with the sampling process, enabling the model to utilize its own output for prediction.

Specifically, during training, upon acquiring $\mathbf{y}_t^{\text{train}}$ as per line 3 in Algorithm 1, we refrain from directly minimizing $\mathcal{L}(\theta)$. Instead, we construct our own prediction of the HR image as $\tilde{\mathbf{y}}_0^{\text{train}}$ according to Eq. (8), formulated as:

$$\begin{aligned}\tilde{\mathbf{y}}_0^{\text{train}} &= \frac{1}{\sqrt{\bar{\alpha}_t}} (\mathbf{y}_t^{\text{train}} - \sqrt{1 - \bar{\alpha}_t} \epsilon_\theta(\mathbf{x}_0, \mathbf{y}_t^{\text{train}}, t)) \\ &= \frac{1}{\sqrt{\bar{\alpha}_t}} (\sqrt{\bar{\alpha}_t} \mathbf{y}_0 + \sqrt{1 - \bar{\alpha}_t} \epsilon_t - \sqrt{1 - \bar{\alpha}_t} \epsilon_\theta(\mathbf{x}_0, \mathbf{y}_t^{\text{train}}, t)) \quad \triangleright \text{line 3} \\ &= \mathbf{y}_0 + \sqrt{(1 - \bar{\alpha}_t) / \bar{\alpha}_t} \Delta \epsilon_{t,\theta}\end{aligned}\quad (9)$$

where $\Delta \epsilon_{t,\theta} = \epsilon_t - \epsilon_\theta(\mathbf{x}_0, \mathbf{y}_t^{\text{train}}, t)$. Utilizing this self-estimated HR image $\tilde{\mathbf{y}}_0^{\text{train}}$, we generate the noisy image $\tilde{\mathbf{y}}_t^{\text{train}}$ to serve as input¹ to the network ϵ_θ once more:

$$\begin{aligned}\tilde{\mathbf{y}}_t^{\text{train}} &= \sqrt{\bar{\alpha}_t} \tilde{\mathbf{y}}_0^{\text{train}} + \sqrt{1 - \bar{\alpha}_t} \epsilon'_t \\ &= \sqrt{\bar{\alpha}_t} \mathbf{y}_0 + \sqrt{1 - \bar{\alpha}_t} (\epsilon'_t + \Delta \epsilon_{t,\theta}),\end{aligned}\quad (10)$$

where $\epsilon'_t \sim \mathcal{N}(\mathbf{0}, \mathbf{I})$. Then, the training objective for this diffusion rectification model (DRM) can be expressed as:

$$\mathcal{L}^{\text{DRM}}(\theta) = \mathbb{E}_{(\mathbf{x}_0, \mathbf{y}_0), \epsilon_t, \epsilon'_t, t} \left\| (\epsilon'_t + \Delta \epsilon_{t,\theta}) - \epsilon_\theta(\mathbf{x}_0, \tilde{\mathbf{y}}_t^{\text{train}}, t) \right\|_1. \quad (11)$$

Essentially, Eq. (11) suggests that this DRM approach strives not only to eliminate the sampled noise ϵ'_t but also to address the error term $\Delta \epsilon_{t,\theta}$ arising from the discrepancy between the imperfect estimation $\tilde{\mathbf{y}}_0^{\text{train}}$ and the ground-truth \mathbf{y}_0 , as seen in Eq. (9); hence the term “rectification”. Notably, leveraging the model’s own prediction during training as in Eq. (10) mirrors the sampling process of DDIM [49] with a particular choice of σ_t , thereby imposing enhanced

¹To match the actual sampling process, there might be a desire to reconstruct $\tilde{\mathbf{y}}_{t-1}^{\text{train}}$, yet this could notably complicate the entire procedure. Nonetheless, we have observed similar performance by simply using $\tilde{\mathbf{y}}_t^{\text{train}}$.

Algorithm 3 Conditional DREAM Training

```

1: repeat
2:    $(\mathbf{x}_0, \mathbf{y}_0) \sim p(\mathbf{x}_0, \mathbf{y}_0), t \sim \mathbb{U}(1, T), \epsilon_t \sim \mathcal{N}(\mathbf{0}, \mathbf{I})$ 
3:   Compute  $\mathbf{y}_t = \sqrt{\bar{\alpha}_t} \mathbf{y}_0 + \sqrt{1 - \bar{\alpha}_t} \epsilon_t$ 
4:   Compute  $\Delta \epsilon_{t,\theta} = \epsilon_t - \text{StopGradient}(\epsilon_\theta(\mathbf{x}_0, \mathbf{y}_t, t))$ 
5:   Compute  $\hat{\mathbf{y}}_t = \mathbf{y}_t + \sqrt{1 - \bar{\alpha}_t} \lambda_t \Delta \epsilon_{t,\theta}$ 
6:   Update  $\theta$  with gradient  $\nabla_\theta \|\epsilon_t + \lambda_t \Delta \epsilon_{t,\theta} - \epsilon_\theta(\mathbf{x}_0, \hat{\mathbf{y}}_t, t)\|_1$ 
7: until converged

```

supervision. We remark that DRM is closely related to the approaches in [21, 45, 46] where they perform similar step-unrolling techniques for perceptual vision tasks or text generation tasks. However, we are the first to tailor it to low-level vision tasks and provide a clear analysis.

Estimation adaptation. While DRM incorporates additional rectification supervision to account for the sampling process, its naive application to the SR task might not deliver satisfactory results. As shown in Figure 4, a distortion-perception tradeoff [4] is observed in the generated SR images. Despite achieving a state-of-the-art PSNR (less distortion), the images produced by DRM tend to be smoother and lack fine details, reflecting a high FID score (poor perception). This is particularly evident when compared to the standard conditional diffusion model, namely SR3 [44]. This limitation could be traced back to DRM’s static self-alignment mechanism, which may inappropriately guide the generated images to regress towards the mean.

To address the issue, and inspired by the powerful generative capability of the standard diffusion model, we propose an estimation adaptation strategy. This aims to harness both the superior quality of standard diffusion and the reduced distortion offered by diffusion rectification. Specifically, rather than naively using our own prediction $\tilde{\mathbf{y}}_0^{\text{train}}$ computed in Eq. (9), we adaptively inject ground-truth information \mathbf{y}_0 by blending it with $\tilde{\mathbf{y}}_0^{\text{train}}$ as follows:

$$\hat{\mathbf{y}}_0 = \lambda_t \tilde{\mathbf{y}}_0^{\text{train}} + (1 - \lambda_t) \mathbf{y}_0, \quad (12)$$

where $\lambda_t \in (0, 1)$ is an increasing function such that $\hat{\mathbf{y}}_0$ emphasizes more on \mathbf{y}_0 at smaller t , aligning with the network’s tendency to achieve more accurate predictions, as observed in Figure 3. Intuitively, as t decreases, $\hat{\mathbf{y}}_0$ closely approximates the ground-truth, making it more beneficial to resemble the standard diffusion, yielding images with realistic details. Conversely, as t increases and the prediction leans towards random noise, it is advantageous to focus more on the estimation itself, effectively aligning the training and sampling processes through the rectification.

Following the adaptive estimation $\hat{\mathbf{y}}_0$ in Eq. (12), we construct the new noisy image $\hat{\mathbf{y}}_t$ similarly as before:

$$\begin{aligned}\hat{\mathbf{y}}_t &= \sqrt{\bar{\alpha}_t} \hat{\mathbf{y}}_0 + \sqrt{1 - \bar{\alpha}_t} \epsilon'_t \\ &= \sqrt{\bar{\alpha}_t} \mathbf{y}_0 + \sqrt{1 - \bar{\alpha}_t} (\epsilon'_t + \lambda_t \Delta \epsilon_{t,\theta}).\end{aligned}\quad (13)$$

Table 1. Comparison on face and general scene datasets against three baselines for various p values, with **best** and **second-best** colorized.

p	CelebA-HQ [23]									DIV2K [1]								
	SR3 [44]			IDM [14]			SR3 [44]			ResShift [62]								
	PSNR↑	SSIM↑	LPIPS↓	PSNR↑	SSIM↑	LPIPS↓	PSNR↑	SSIM↑	LPIPS↓	PSNR↑	SSIM↑	LPIPS↓	FID↓	PSNR↑	SSIM↑	LPIPS↓	FID↓	
0 (DRM)	25.04	0.76	0.204	77.51	25.06	0.76	0.188	67.46	28.67	0.81	0.189	16.72	29.98	0.83	0.233	17.76		
1 (DREAM)	24.63	0.74	0.177	56.01	24.50	0.73	0.167	53.22	28.10	0.79	0.121	14.32	29.24	0.80	0.158	16.23		
2 (DREAM)	24.62	0.74	0.180	61.72	24.32	0.72	0.169	55.38	28.06	0.79	0.140	15.54	28.77	0.79	0.134	15.72		
3 (DREAM)	24.15	0.71	0.182	58.89	24.09	0.72	0.172	54.04	27.88	0.79	0.123	14.83	28.44	0.79	0.124	15.67		
∞ (standard)	23.85	0.71	0.184	61.98	24.01	0.71	0.172	56.01	27.02	0.76	0.121	16.72	25.30	0.68	0.211	25.91		

Finally, the training objective for our full *Diffusion Rectification and Estimation-Adaptive Model (DREAM)* can be expressed as:

$$\mathcal{L}^{\text{DREAM}}(\theta) = \mathbb{E}_{(\mathbf{x}_0, \mathbf{y}_0), \epsilon_t, \epsilon'_t, t} \|(\epsilon'_t + \lambda_t \Delta \epsilon_{t,\theta}) - \epsilon_\theta(\mathbf{x}_0, \hat{\mathbf{y}}_t, t)\|_1. \quad (14)$$

Choice of λ_t . Comparing Eq. (14) with Eq. (11), the key difference lies in the introduction of λ_t for adaptively modulating the intensity of the rectification term $\Delta \epsilon_{t,\theta}$. Note that we only need $\lambda_t \in (0, 1)$ to be increasing to leverage the benefits of both standard diffusion and rectification. In practice, we set $\lambda_t = (\sqrt{1 - \bar{\alpha}_t})^p$, where p adds an extra layer of flexibility: at $p = 0$, λ_t remains at 1, reverting the method to DRM with consistent static rectification; as $p \rightarrow \infty$, $\lambda_t \rightarrow 0$, transitioning our approach towards the standard diffusion model. As shown in Figure 4, the images produced by DREAM with $p = 1$ achieve a superior balance between perception and distortion, significantly outperforming the standard SR3 [44] across both metrics.

Training details. It's important to highlight that while the same network ϵ_θ is utilized for calculating both the rectification term $\Delta \epsilon_{t,\theta}$ and the predicted noise $\epsilon_\theta(\mathbf{x}_0, \hat{\mathbf{y}}_t, t)$ in Eq. (14), a key distinction exists: we refrain from propagating the gradient when computing $\Delta \epsilon_{t,\theta}$, and thus, it is derived from the frozen network. The actual supervision is imposed following its adaptive adjustment. Moreover, we empirically observe that using the same Gaussian noise (*i.e.*, $\epsilon_t \equiv \epsilon'_t$) in DREAM yields superior performance, further simplifying Eq. (13) to:

$$\hat{\mathbf{y}}_t = \mathbf{y}_t^{\text{train}} + \sqrt{1 - \bar{\alpha}_t} \lambda_t \Delta \epsilon_{t,\theta}. \quad (15)$$

We summarize our DREAM framework in Algorithm 3, tailored for enhanced diffusion training, while Algorithm 2 remains applicable for sampling purposes.

4. Experiments

4.1. Implementation details

Baselines and datasets. Our experiments involve three diffusion-based SR methods as baselines, spanning datasets for faces, general scenes, and natural images. For face im-

Table 2. Quantitative comparison for 16×16 to 128×128 face super-resolution on CelebA-HQ [23]. Consistency measures the MSE ($\times 10^{-5}$) between LR and downsampled SR images.

Method	PSNR↑	SSIM↑	Consistency↓
PULSE [36]	16.88	0.44	161.1
FSRGAN [6]	23.85	0.71	33.8
Regression [44]	23.96	0.69	2.71
SR3 [44]	23.85	0.71	2.33
IDM [14]	24.01	0.71	2.14
SR3 [44]+DREAM	24.63	0.74	2.12
IDM [14]+DREAM	24.50	0.73	1.26

age datasets, we adopt SR3² [44] and IDM [14] as baselines, with training conducted on FFHQ [25] and evaluations on CelebA-HQ [23]. For general scenes, we use the DIV2K dataset [1], employing SR3 [44] and ResShift [62] as baseline models. Notably, SR3 and IDM operate in pixel space, whereas ResShift³ conducts diffusion process in latent space. In addition, to assess out-of-distribution (OOD) performance, we train SR3 as baseline on the DIV2K dataset and evaluate on CAT [66] and LSUN datasets [60].

4.2. Results and analysis

Effect of p in λ_t . In DREAM implementation, we set $\lambda_t = (\sqrt{1 - \bar{\alpha}_t})^p$, where p manages the balance between ground-truth and self-estimation data as in Eq. (12). We conduct experiments with three baselines (SR3, IDM and ResShift) for $8 \times$ face SR on CelebA-HQ and $4 \times$ general scene SR on DIV2K at various p settings, as shown in Table 1. Baselines use the standard diffusion process ($p \rightarrow \infty$). For $p = 0$ ($\lambda_t \equiv 1$), corresponding to the DRM model in Eq. (11), there is a notable reduction in distortion (higher PSNR and SSIM), but at the cost of perceptual quality (lower LPIPS and FID), confirming our findings in Figure 4. Increasing p to 1 (our full DREAM approach) leads to a slight decrease in distortion but significantly improves the balance between distortion and perception. Further increase in p shows continual distortion degradation, while perceptual quality initially improves then declines. *DREAM*

²Due to the unavailability of official code, we use a widely-recognized implementation [link].

³To ensure consistency across baselines, we standardize the transition kernel to align with DDPM's approach for noise prediction.

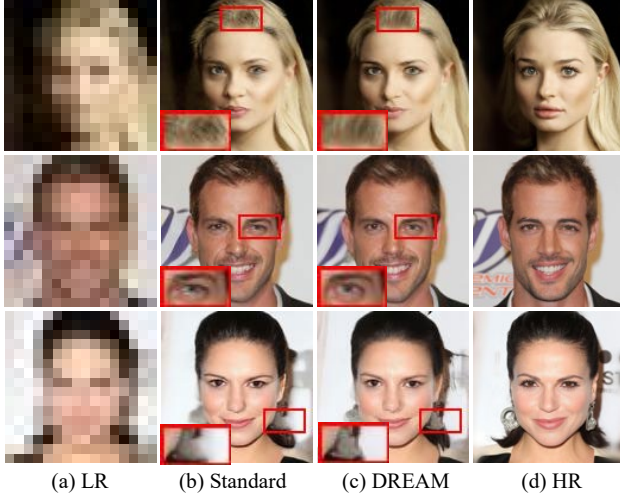


Figure 5. Qualitative comparison for $8\times$ SR using IDM [14] on the CelebA-HQ dataset [23]. Results highlight DREAM’s superior fidelity and enhanced identity preservation, leading to more realistic detail generation in features like hair, eyes, and rings.

demonstrates clear advantages over baseline models across all metrics. We found $p = 1$ yields the *best* overall performance compared to other p values and baselines, making it our choice for subsequent experiments.

Face super-resolution. Figures 4 and 5 show qualitative comparisons for face super-resolution from 16×16 to 128×128 , applying our DREAM approach to state-of-the-art diffusion-based methods, SR3 and IDM. While SR3 and IDM generally have decent image qualities, they often miss intricate facial details like hair and eyes, resulting in somewhat unrealistic appearance, and even omit accessories like rings. In contrast, our DREAM approach operated on the these baseline more faithfully preserves facial identity and details. Table 2 shows a quantitative comparison of our DREAM approach applied to SR3 and IDM against other methods, using metrics such as PSNR, SSIM, and consistency [44]. While GAN-based models are known for their fidelity to human perception at higher SR scales, their lower consistency scores suggest a notable deviation from the original LR images. Applying DREAM to SR3 and IDM, we observe considerable enhancements across all metrics. Notably, the simpler SR3, a pure conditional DDPM, when augmented with DREAM, outperforms the more complex IDM, underscoring DREAM’s effectiveness.

General scene super-resolution. Figure 6 shows a visual comparison of $4\times$ SR results on the DIV2K dataset [1], using our DREAM approach against standard diffusion methods, with SR3 and ResShift as baselines. Standard training tends to produce images with blurred details and compromised realism, evident in unclear window outlines and distorted shirt textures. In contrast, DREAM maintains structural integrity and delivers more realistic textures. Following [17], we conduct a comprehensive com-



Figure 6. Qualitative comparison for $4\times$ SR on DIV2K [1]. Top with SR3 [44] the baseline; bottom with ResShift [62] the baseline.

Table 3. Quantitative comparison for $4\times$ SR on DIV2K. All models are trained on DIV2K plus Flickr2K [52]. The **best** and **second-best** results among generative models are colorized.

Method	PSNR↑	SSIM↑	LPIPS↓
Bicubic	26.7	0.77	0.409
Reg.-based	EDSR [34]	28.98	0.83
	RRDB [57]	29.44	0.84
GAN-based	ESRGAN [57]	26.22	0.75
	RankSRGAN [67]	26.55	0.75
Flow-based	SRFlow [35]	27.09	0.76
	HCFlow [32]	27.02	0.76
Flow+GAN	HCFlow++ [32]	26.61	0.74
	SR3 [44]	27.02	0.76
Diffusion	SR3 [44]+DREAM	28.10	0.79
	ResShift [62]	25.30	0.68
	ResShift [62]+DREAM	28.44	0.79

parison with various regression-based and generative methods on the DIV2K dataset. The results, detailed in Table 3 and benchmarked against models from [32], demonstrate DREAM’s effectiveness. Notably, DREAM has led to an increase of 1.08dB and 3.14dB in PSNR, and improvements of 0.03 and 0.11 in SSIM for SR3 and ResShift, respectively, outperforming other generative methods. Moreover, these methods demonstrate comparable or superior performance in perceptual quality metrics, marked by a 0.087 reduction in LPIPS for ResShift. Although LPIPS scores are not as favorable as those obtained by HCFlow++, even with DREAM applied, further improvements in image quality could be achieved through advanced network designs and incorporating GAN loss, as in HCFlow++. However, such approaches are orthogonal to DREAM, and we leave these explorations for future work.

4.3. Training and sampling acceleration

The DREAM strategy not only improves SR image quality but also accelerates the training. As shown in Figure 1, DREAM reaches convergence at around 100k to

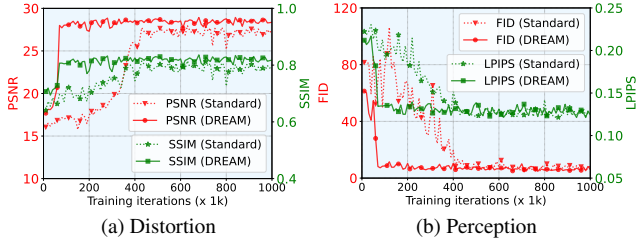


Figure 7. Evolution of distortion metrics (left) and perceptual metrics (right) using SR3 as a baseline on the DIV2K dataset.

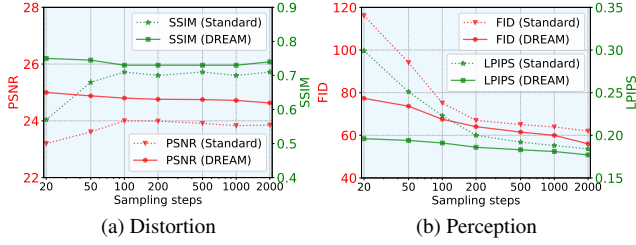


Figure 8. Comparison of distortion metrics (left) and perception metrics (right) with varying sampling steps, using SR3 as a baseline on the CelebA-HQ dataset.

150k iterations, a significant improvement over the standard diffusion-based SR3’s 400k iterations. Moreover, Figure 7 illustrates the evolution of training in terms of distortion metrics (PSNR and SSIM) and perception metrics (LPIPS and FID) using SR3 as the baseline on the DIV2K dataset. DREAM not only converges faster but also surpasses SR3’s final results before its own convergence. For example, DREAM achieves a PSNR of 28.07 and FID of 14.72 at just 470k iterations, while the baseline SR3 with standard diffusion reaches PSNR 27.02 and FID 16.72 after full convergence at 980k iterations, indicating a $2\times$ *speedup in training*. Additional experiments with different baselines and datasets can be found in the appendix.

Moreover, DREAM considerably accelerates the sampling process, outperforming standard diffusion training with fewer sampling steps. Figure 8 demonstrates this using SR3 on the CelebA-HQ dataset, comparing SR images generated with varying sampling steps in terms of both distortion and perception metrics. While the standard baseline typically requires an entire 2000 sampling steps, DREAM achieves improved distortion metrics (0.73 v.s. 0.71 in SSIM) and comparable perceptual quality (0.189 v.s. 0.184 in LPIPS) with only 100 steps. This marks a substantial $20\times$ *speedup in sampling*. More details and results are available in the appendix.

4.4. Out-of-distribution (OOD) evaluations

To evaluate our approach’s OOD performance, we train the SR3 model on DIV2K for $4\times$ SR scaling, then evaluate its performance on various natural image datasets from the CAT [66] and LSUN [60] benchmarks, covering multiple SR scales. This OOD evaluation encompasses both

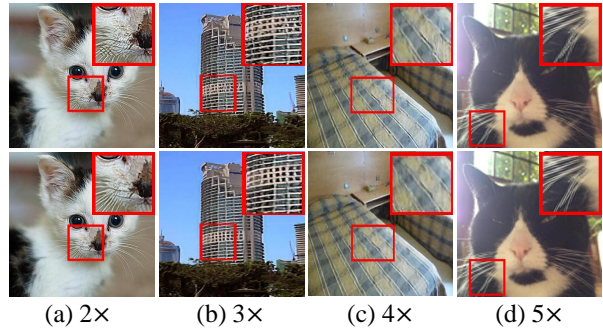


Figure 9. Visual comparison of OOD SR. We use SR3 as a baseline, pretrain it on DIV2K and evaluate on CAT and LSUN, across various scales. The top row is obtained using standard training for SR3; the bottom row is generated using DREAM on SR3.

Table 4. Quantitative comparison of OOD SR on CAT and LSUN Bedroom and Tower validation sets at various scales.

Scale	Cats	Towers	Bedrooms
2 \times	Standard 19.72/0.398	18.82/0.333	20.20/0.314
	DREAM 22.50/0.337	20.89/0.288	22.15/0.278
3 \times	Standard 22.48/0.281	18.42/0.266	20.14/0.235
	DREAM 23.90/0.265	19.35/0.252	20.65/0.231
4 \times	Standard 26.49/0.257	24.03/0.217	26.89/0.187
	DREAM 27.19/0.246	24.94/0.212	27.53/0.183
5 \times	Standard 24.52/0.381	21.79/0.331	23.18/0.313
	DREAM 24.58/0.373	21.84/0.324	23.19/0.310

dataset diversity and scaling differences. As shown in Figure 9, our DREAM training approach significantly enhances model robustness, producing more realistic and clearer images across different scales. For instance, it captures finer details such as the beard of cats at $2\times$ and $5\times$ scales, the structural integrity of a tower at $3\times$ scale, and the intricate wrinkles on a bed at $4\times$ scale. Following [14], Table 4 presents the average PSNR and LPIPS metrics for 100 selected images from these validation datasets. Our findings show that the DREAM training framework consistently improves baseline model across diverse datasets and scales.

5. Conclusion

This paper introduces DREAM, a novel training framework designed to address the training-sampling discrepancy in conditional diffusion models with minimal code modifications. DREAM comprises two key components: diffusion rectification and estimation adaptation. Diffusion rectification extends the existing training framework for diffusion models by aligning training more closely with sampling through self-estimation. Estimation adaptation optimizes the balance between accuracy and fidelity by adaptively incorporating ground-truth information. When applied to SISR tasks, DREAM effectively bridges the gap between training and sampling. Extensive experiments demonstrate

that DREAM enhances distortion and perception metrics across various diffusion-based SR baselines. It also speeds up training, improves sampling efficiency, and achieves robust OOD performance across diverse datasets and scales.

While DREAM is mainly utilized for SR in this work, its capabilities are applicable to a range of dense visual prediction tasks. Future research may investigate its use in both low-level vision tasks, such as inpainting and deblurring, and high-level vision tasks like semantic segmentation and depth estimation. Additionally, exploring DREAM’s application in both unconditional and conditional image generation presents an intriguing direction for future work.

References

- [1] Eirikur Agustsson and Radu Timofte. Ntire 2017 challenge on single image super-resolution: Dataset and study. In *Proceedings of the IEEE conference on computer vision and pattern recognition workshops*, pages 126–135, 2017. [6](#), [7](#), [1](#), [2](#), [3](#), [4](#), [5](#)
- [2] Saeed Anwar and Nick Barnes. Densely residual laplacian super-resolution. *IEEE Transactions on Pattern Analysis and Machine Intelligence*, 44(3):1192–1204, 2020. [2](#)
- [3] Marco Bevilacqua, Aline Roumy, Christine Guillemot, and Marie Line Alberi-Morel. Low-complexity single-image super-resolution based on nonnegative neighbor embedding. 2012. [1](#)
- [4] Yochai Blau and Tomer Michaeli. The perception-distortion tradeoff. In *Proceedings of the IEEE conference on computer vision and pattern recognition*, pages 6228–6237, 2018. [5](#)
- [5] Kelvin CK Chan, Xintao Wang, Xiangyu Xu, Jinwei Gu, and Chen Change Loy. Glean: Generative latent bank for large-factor image super-resolution. In *Proceedings of the IEEE/CVF conference on computer vision and pattern recognition*, pages 14245–14254, 2021. [2](#)
- [6] Yu Chen, Ying Tai, Xiaoming Liu, Chunhua Shen, and Jian Yang. Fsrnet: End-to-end learning face super-resolution with facial priors. In *Proceedings of the IEEE conference on computer vision and pattern recognition*, pages 2492–2501, 2018. [6](#)
- [7] Yinbo Chen, Sifei Liu, and Xiaolong Wang. Learning continuous image representation with local implicit image function. In *Proceedings of the IEEE/CVF conference on computer vision and pattern recognition*, pages 8628–8638, 2021. [1](#)
- [8] Prafulla Dhariwal and Alexander Nichol. Diffusion models beat gans on image synthesis. *Advances in neural information processing systems*, 34:8780–8794, 2021. [2](#)
- [9] Tianyu Ding, Luming Liang, Zhihui Zhu, and Ilya Zharkov. Cdfi: Compression-driven network design for frame interpolation. In *Proceedings of the IEEE/CVF conference on computer vision and pattern recognition*, pages 8001–8011, 2021. [2](#)
- [10] Tianyu Ding, Luming Liang, Zhihui Zhu, Tianyi Chen, and Ilya Zharkov. Sparsity-guided network design for frame interpolation. *arXiv preprint arXiv:2209.04551*, 2022. [2](#)
- [11] Laurent Dinh, Jascha Sohl-Dickstein, and Samy Bengio. Density estimation using real NVP. *arXiv:1605.08803*, 2016. [1](#), [2](#)
- [12] Chao Dong, Chen Change Loy, Kaiming He, and Xiaoou Tang. Learning a deep convolutional network for image super-resolution. In *Computer Vision–ECCV 2014: 13th European Conference, Zurich, Switzerland, September 6–12, 2014, Proceedings, Part IV 13*, pages 184–199. Springer, 2014. [1](#)
- [13] Martin Nicolas Everaert, Athanasios Fitsios, Marco Bocchio, Sami Arpa, Sabine Süsstrunk, and Radhakrishna Achanta. Exploiting the signal-leak bias in diffusion models. *arXiv preprint arXiv:2309.15842*, 2023. [2](#)
- [14] Sicheng Gao, Xuhui Liu, Bohan Zeng, Sheng Xu, Yanjing Li, Xiaoyan Luo, Jianzhuang Liu, Xiantong Zhen, and Baochang Zhang. Implicit diffusion models for continuous super-resolution. In *Proceedings of the IEEE/CVF Conference on Computer Vision and Pattern Recognition*, pages 10021–10030, 2023. [1](#), [2](#), [6](#), [7](#), [8](#), [3](#)
- [15] Zhicheng Geng, Luming Liang, Tianyu Ding, and Ilya Zharkov. Rstt: Real-time spatial temporal transformer for space-time video super-resolution. In *Proceedings of the IEEE/CVF Conference on Computer Vision and Pattern Recognition*, pages 17441–17451, 2022. [2](#)
- [16] Ian J Goodfellow, Jean Pouget-Abadie, Mehdi Mirza, Bing Xu, David Warde-Farley, Sherjil Ozair, Aaron Courville, and Yoshua Bengio. Generative Adversarial Networks. *NIPS*, 2014. [1](#)
- [17] Baisong Guo, Xiaoyun Zhang, Haoning Wu, Yu Wang, Ya Zhang, and Yan-Feng Wang. Lar-sr: A local autoregressive model for image super-resolution. In *Proceedings of the IEEE/CVF Conference on Computer Vision and Pattern Recognition*, pages 1909–1918, 2022. [2](#), [7](#)
- [18] Martin Heusel, Hubert Ramsauer, Thomas Unterthiner, Bernhard Nessler, and Sepp Hochreiter. Gans trained by a two time-scale update rule converge to a local nash equilibrium. *Advances in neural information processing systems*, 30, 2017. [1](#)
- [19] Jonathan Ho, Ajay Jain, and Pieter Abbeel. Denoising diffusion probabilistic models. *Advances in neural information processing systems*, 33:6840–6851, 2020. [1](#), [2](#), [3](#), [4](#)
- [20] Jonathan Ho, Chitwan Saharia, William Chan, David J Fleet, Mohammad Norouzi, and Tim Salimans. Cascaded diffusion models for high fidelity image generation. *The Journal of Machine Learning Research*, 23(1):2249–2281, 2022. [1](#)
- [21] Yuanfeng Ji, Zhe Chen, Enze Xie, Lanqing Hong, Xihui Liu, Zhaoqiang Liu, Tong Lu, Zhenguo Li, and Ping Luo. Ddp: Diffusion model for dense visual prediction. *arXiv preprint arXiv:2303.17559*, 2023. [3](#), [5](#)
- [22] Younghyun Jo, Seoung Wug Oh, Peter Vajda, and Seon Joo Kim. Tackling the ill-posedness of super-resolution through adaptive target generation. In *Proceedings of the IEEE/CVF Conference on Computer Vision and Pattern Recognition*, pages 16236–16245, 2021. [2](#)
- [23] Tero Karras, Timo Aila, Samuli Laine, and Jaakko Lehtinen. Progressive growing of gans for improved quality, stability, and variation. *arXiv preprint arXiv:1710.10196*, 2017. [5](#), [6](#), [7](#), [1](#), [3](#)

[24] Tero Karras, Timo Aila, Samuli Laine, and Jaakko Lehtinen. Progressive growing of gans for improved quality, stability, and variation. In *ICLR*, 2018. 1

[25] Tero Karras, Samuli Laine, and Timo Aila. A style-based generator architecture for generative adversarial networks. In *Proceedings of the IEEE/CVF conference on computer vision and pattern recognition*, pages 4401–4410, 2019. 4, 6

[26] Diederik P. Kingma and Prafulla Dhariwal. Glow: Generative Flow with Invertible 1x1 Convolutions. In *NIPS*, 2018. 1, 2

[27] Diederik P Kingma and Max Welling. Auto-Encoding Variational Bayes. In *ICLR*, 2013. 1, 2

[28] Christian Ledig, Lucas Theis, Ferenc Huszár, Jose Caballero, Andrew Cunningham, Alejandro Acosta, Andrew Aitken, Alykhan Tejani, Johannes Totz, Zehan Wang, et al. Photo-realistic single image super-resolution using a generative adversarial network. In *Proceedings of the IEEE conference on computer vision and pattern recognition*, pages 4681–4690, 2017. 2

[29] Haoying Li, Yifan Yang, Meng Chang, Shiqi Chen, Huajun Feng, Zhihai Xu, Qi Li, and Yueling Chen. Srdiff: Single image super-resolution with diffusion probabilistic models. *Neurocomputing*, 479:47–59, 2022. 2, 1

[30] Mingxiao Li, Tingyu Qu, Wei Sun, and Marie-Francine Moens. Alleviating exposure bias in diffusion models through sampling with shifted time steps. *arXiv preprint arXiv:2305.15583*, 2023. 2

[31] Jingyun Liang, Jiezhang Cao, Guolei Sun, Kai Zhang, Luc Van Gool, and Radu Timofte. Swinir: Image restoration using swin transformer. In *Proceedings of the IEEE/CVF international conference on computer vision*, pages 1833–1844, 2021. 1, 2

[32] Jingyun Liang, Andreas Lugmayr, Kai Zhang, Martin Danelljan, Luc Van Gool, and Radu Timofte. Hierarchical conditional flow: A unified framework for image super-resolution and image rescaling. In *Proceedings of the IEEE/CVF International Conference on Computer Vision*, pages 4076–4085, 2021. 7

[33] Jie Liang, Hui Zeng, and Lei Zhang. Details or artifacts: A locally discriminative learning approach to realistic image super-resolution. In *Proceedings of the IEEE/CVF Conference on Computer Vision and Pattern Recognition*, pages 5657–5666, 2022. 1, 2

[34] Bee Lim, Sanghyun Son, Heewon Kim, Seungjun Nah, and Kyoung Mu Lee. Enhanced deep residual networks for single image super-resolution. In *Proceedings of the IEEE conference on computer vision and pattern recognition workshops*, pages 136–144, 2017. 1, 2, 7

[35] Andreas Lugmayr, Martin Danelljan, Luc Van Gool, and Radu Timofte. Srfow: Learning the super-resolution space with normalizing flow. In *Computer Vision–ECCV 2020: 16th European Conference, Glasgow, UK, August 23–28, 2020, Proceedings, Part V 16*, pages 715–732. Springer, 2020. 7

[36] Sachit Menon, Alexandru Damian, Shijia Hu, Nikhil Ravi, and Cynthia Rudin. Pulse: Self-supervised photo upsampling via latent space exploration of generative models. In *Proceedings of the ieee/cvf conference on computer vision and pattern recognition*, pages 2437–2445, 2020. 6, 1

[37] Alexander Quinn Nichol and Prafulla Dhariwal. Improved denoising diffusion probabilistic models. In *International Conference on Machine Learning*, pages 8162–8171. PMLR, 2021. 2

[38] Mang Ning, Mingxiao Li, Jianlin Su, Albert Ali Salah, and Itir Onal Ertugrul. Elucidating the exposure bias in diffusion models. *arXiv preprint arXiv:2308.15321*, 2023. 2

[39] Mang Ning, Enver Sangineto, Angelo Porrello, Simone Calderara, and Rita Cucchiara. Input perturbation reduces exposure bias in diffusion models. *arXiv preprint arXiv:2301.11706*, 2023. 2

[40] Aäron van den Oord, Sander Dieleman, Heiga Zen, Karen Simonyan, Oriol Vinyals, Alex Graves, Nal Kalchbrenner, Andrew Senior, and Koray Kavukcuoglu. WaveNet: A Generative Model for Raw Audio. *arXiv preprint arXiv:1609.03499*, 2016. 1

[41] Aäron van den Oord, Nal Kalchbrenner, Oriol Vinyals, Lasse Espeholt, Alex Graves, and Koray Kavukcuoglu. Conditional Image Generation with PixelCNN Decoders. In *NIPS*, 2016. 1, 2

[42] Alec Radford, Luke Metz, and Soumith Chintala. Unsupervised representation learning with deep convolutional generative adversarial networks. *arXiv preprint arXiv:1511.06434*, 2015. 1

[43] Robin Rombach, Andreas Blattmann, Dominik Lorenz, Patrick Esser, and Björn Ommer. High-resolution image synthesis with latent diffusion models. In *Proceedings of the IEEE/CVF conference on computer vision and pattern recognition*, pages 10684–10695, 2022. 1, 2

[44] Chitwan Saharia, Jonathan Ho, William Chan, Tim Salimans, David J Fleet, and Mohammad Norouzi. Image super-resolution via iterative refinement. *IEEE Transactions on Pattern Analysis and Machine Intelligence*, 45(4):4713–4726, 2022. 1, 2, 3, 4, 5, 6, 7

[45] Nikolay Savinov, Junyoung Chung, Mikolaj Binkowski, Erich Elsen, and Aaron van den Oord. Step-unrolled denoising autoencoders for text generation. In *International Conference on Learning Representations*, 2022. 3, 5

[46] Saurabh Saxena, Abhishek Kar, Mohammad Norouzi, and David J Fleet. Monocular depth estimation using diffusion models. *arXiv preprint arXiv:2302.14816*, 2023. 3, 5

[47] Jae Woong Soh, Gu Yong Park, Junho Jo, and Nam Ik Cho. Natural and realistic single image super-resolution with explicit natural manifold discrimination. In *Proceedings of the IEEE/CVF conference on computer vision and pattern recognition*, pages 8122–8131, 2019. 2

[48] Jascha Sohl-Dickstein, Eric Weiss, Niru Maheswaranathan, and Surya Ganguli. Deep unsupervised learning using nonequilibrium thermodynamics. In *International conference on machine learning*, pages 2256–2265. PMLR, 2015. 1, 2, 3

[49] Jiaming Song, Chenlin Meng, and Stefano Ermon. Denoising diffusion implicit models. In *International Conference on Learning Representations*, 2021. 2, 5

[50] Jian Sun, Zongben Xu, and Heung-Yeung Shum. Gradient profile prior and its applications in image super-resolution

and enhancement. *IEEE Transactions on Image Processing*, 20(6):1529–1542, 2010. 1

[51] Christian Szegedy, Vincent Vanhoucke, Sergey Ioffe, Jon Shlens, and Zbigniew Wojna. Rethinking the inception architecture for computer vision. In *Proceedings of the IEEE conference on computer vision and pattern recognition*, pages 2818–2826, 2016. 1

[52] Radu Timofte, Eirikur Agustsson, Luc Van Gool, Ming-Hsuan Yang, and Lei Zhang. Ntire 2017 challenge on single image super-resolution: Methods and results. In *Proceedings of the IEEE conference on computer vision and pattern recognition workshops*, pages 114–125, 2017. 7, 1, 2

[53] Arash Vahdat and Jan Kautz. NVAE: A deep hierarchical variational autoencoder. In *NeurIPS*, 2020. 1, 2

[54] Aäron Van Den Oord, Nal Kalchbrenner, and Koray Kavukcuoglu. Pixel recurrent neural networks. In *International conference on machine learning*, pages 1747–1756. PMLR, 2016. 2

[55] Aaron Van Den Oord, Oriol Vinyals, et al. Neural discrete representation learning. *Advances in neural information processing systems*, 30, 2017. 2

[56] Xintao Wang, Ke Yu, Chao Dong, and Chen Change Loy. Recovering realistic texture in image super-resolution by deep spatial feature transform. In *Proceedings of the IEEE conference on computer vision and pattern recognition*, pages 606–615, 2018. 2

[57] Xintao Wang, Ke Yu, Shixiang Wu, Jinjin Gu, Yihao Liu, Chao Dong, Yu Qiao, and Chen Change Loy. Esrgan: Enhanced super-resolution generative adversarial networks. In *Proceedings of the European conference on computer vision (ECCV) workshops*, pages 0–0, 2018. 2, 7

[58] Zhou Wang, Alan C Bovik, Hamid R Sheikh, and Eero P Simoncelli. Image quality assessment: from error visibility to structural similarity. *IEEE transactions on image processing*, 13(4):600–612, 2004. 1

[59] Qing Yan, Yi Xu, Xiaokang Yang, and Truong Q Nguyen. Single image superresolution based on gradient profile sharpness. *IEEE Transactions on Image Processing*, 24(10):3187–3202, 2015. 1

[60] Fisher Yu, Ari Seff, Yinda Zhang, Shuran Song, Thomas Funkhouser, and Jianxiong Xiao. Lsun: Construction of a large-scale image dataset using deep learning with humans in the loop. *arXiv preprint arXiv:1506.03365*, 2015. 6, 8

[61] Hu Yu, Li Shen, Jie Huang, Man Zhou, Hongsheng Li, and Feng Zhao. Debias the training of diffusion models. *arXiv preprint arXiv:2310.08442*, 2023. 2

[62] Zongsheng Yue, Jianyi Wang, and Chen Change Loy. Resshift: Efficient diffusion model for image super-resolution by residual shifting. In *Thirty-seventh Conference on Neural Information Processing Systems*, 2023. 1, 2, 3, 6, 7, 5

[63] Kai Zhang, Luc Van Gool, and Radu Timofte. Deep unfolding network for image super-resolution. In *Proceedings of the IEEE/CVF conference on computer vision and pattern recognition*, pages 3217–3226, 2020. 2

[64] Kai Zhang, Jingyun Liang, Luc Van Gool, and Radu Timofte. Designing a practical degradation model for deep blind image super-resolution. In *Proceedings of the IEEE/CVF International Conference on Computer Vision*, pages 4791–4800, 2021. 2

[65] Richard Zhang, Phillip Isola, Alexei A Efros, Eli Shechtman, and Oliver Wang. The unreasonable effectiveness of deep features as a perceptual metric. In *Proceedings of the IEEE conference on computer vision and pattern recognition*, pages 586–595, 2018. 2, 4

[66] Weiwei Zhang, Jian Sun, and Xiaou Tang. Cat head detection—how to effectively exploit shape and texture features. In *Computer Vision–ECCV 2008: 10th European Conference on Computer Vision, Marseille, France, October 12–18, 2008, Proceedings, Part IV 10*, pages 802–816. Springer, 2008. 6, 8

[67] Wenlong Zhang, Yihao Liu, Chao Dong, and Yu Qiao. Ranksrgan: Generative adversarial networks with ranker for image super-resolution. In *Proceedings of the IEEE/CVF International Conference on Computer Vision*, pages 3096–3105, 2019. 7

[68] Yulun Zhang, Kunpeng Li, Kai Li, Lichen Wang, Bineng Zhong, and Yun Fu. Image super-resolution using very deep residual channel attention networks. In *Proceedings of the European conference on computer vision (ECCV)*, pages 286–301, 2018. 2

[69] Yulun Zhang, Yapeng Tian, Yu Kong, Bineng Zhong, and Yun Fu. Residual dense network for image super-resolution. In *Proceedings of the IEEE conference on computer vision and pattern recognition*, pages 2472–2481, 2018. 1, 2

DREAM: Diffusion Rectification and Estimation-Adaptive Models

Supplementary Material

In this supplementary material, we begin by describing more details of the evaluation metrics and experiment setup in Section 6. In following Section 7, we present more quantitative comparisons and visualization results on various baselines and datasets, which further demonstrates the effectiveness of our DREAM strategy. We conclude with a discussion of the ethical implications in Section 8.

6. Metrics and setups

We provide a more comprehensive explanation of the metrics and the experiment settings employed in the main text of the paper.

6.1. Metrics

In this section, we will detail the metrics applied to measure image distortion and perception quality. The distortion metrics encompass Peak Signal-to-Noise Ratio (PSNR) and Structural Similarity Index Measure (SSIM), as well as Consistency the the perception measurement include the Learned Perceptual Image Patch Similarity (LPIPS) and the Fréchet Inception Distance (FID).

Peak Signal-to-Noise Ratio (PSNR). PSNR is an indicator of image reconstruction quality. However, its value in decibels (dB) presents certain constraints when assessing super-resolution tasks [36]. Thus, it acts merely as a referential metric of image quality, comparing the maximum possible signal to the level of background noise. Generally, a higher PSNR suggests a lower degree of image distortion.

Structure Similarity Index Measure (SSIM). Building on the image distortion modeling framework [58], the SSIM applies the principles of structural similarity, mirroring the functionality of the human visual system. It is adept at detecting local structural alterations within an image. SSIM measures image attributes such as luminance, contrast, and structure by employing the mean for luminance assessment, variance for contrast evaluation, and covariance to gauge structural integrity.

Consistency. Consistency is measured by calculating the MSE ($\times 10^{-5}$) between the low-resolution inputs and their corresponding downsampled super-resolution outputs.

Learned Perceptual Image Patch Similarity (LPIPS). LPIPS evaluates the perceptual resemblance between generated images and their authentic counterparts by analyzing deep feature representations.

Fréchet Inception Distance score (FID). FID [18] assesses image quality by emulating human judgment of image resemblance. This is achieved by utilizing a pre-trained Inception-V3 network [51] to contrast the distribution pat-

terns of the generated images against the distributions of the original, ground-truth images.

6.2. Setups

In this section, we will provide detailed descriptions of the configurations for various baseline models as well as the datasets utilized in our experiments.

SR3 model on face dataset. We train the SR3 [44] model on an upscaled $8 \times$ FFHQ dataset for 1M iterations and evaluate on 100 images from the CelebA [23] validation dataset. During training, the LR images are consistently resized to 16×16 pixels, while the HR counterparts are scaled to 128×128 pixels. For the SR image generation, the LR images are first upscaled to 128×128 pixels using bicubic interpolation and serve as the conditioning input. In alignment with the DDPM [19], the Adam optimizer is utilized with a fixed learning rate of 1e-4 through the training phase. The training employs a batch size of 4, incorporates a dropout rate of 0.2, and utilizes a linear beta scheduler over 2000 steps with a starting value of 10^{-6} and a final value of 10^{-2} . A single 24GB NVIDIA RTX A5000 GPU is used under this situation.

IDM model on face dataset. Adhering to the offical implementation of the IDM [14], the model is trained on a $8 \times$ FFHQ dataset for 1M iterations and evaluated on 100 images from the CelebA [23] validation dataset. Specifically, throughout training, LR images are consistently resized to 16×16 pixels, while their HR counterparts are scaled to 128×128 pixels. These LR images are then processed through a specialized LR conditioning network, which is stacked with a series of convolutional layers, bilinear down-sampling filtering, and leaky ReLU activation to extract a hierarchy of multi-resolution features. These features are then employed as the conditioning input for the denoising network. The training employs the Adam optimizer with a constant learning rate of 10^{-4} , a batch size of 32, and a dropout rate of 0.2. We implement a linear beta scheduler that advances over 2000 steps, starting from 10^{-6} and escalating to 10^{-2} . This setup is supported by two 24GB NVIDIA RTX A5000.

SR3 model on general scene dataset. We train the SR3 [44] model on upscaled $4 \times$ the training dataset comprising DIV2K [1] and Flickr2K [52] for 1M iterations. Consistent with the SRDiff [29], each image is cropped into patches of 160×160 as the HR ground truths. To produce the corresponding LR image patches of 40×40 pixels, the HR image patches are downsampled using a bicubic kernel. These LR image patches are then resized back to the HR dimensions using bicubic interpolation and are used as

Table 5. Comparison of training time by using different baselines and datasets. The value denotes the ratio of DREAM/standard.

Ratio	Face		DIV2K	
	SR3 [44]	IDM [14]	SR3 [44]	ResShift [62]
	1.38	1.21	1.24	1.08

the conditioning input for the super-resolution process. For evaluation, the entire DIV2K validation set, consisting of 100 images, is utilized. The HR images are downsampled using a bicubic kernel to generate LR images, which are then cropped into 40×40 pixel patches with a 5-pixel overlap between adjacent patches. The SR3 model is applied to these LR patches to yield the SR predictions which are subsequently merged to form the final SR images. The model’s training utilizes the Adam optimizer with a steady learning rate of 10^{-4} , a batch size of 32 patches, and a dropout rate of 0.2. A linear beta scheduler is applied over 1000 steps, initiating at 10^{-6} and culminating at 10^{-2} . This configuration is executed on two 24GB NVIDIA RTX A5000 GPUs.

ResShift on general scene dataset. Training the ResShift model [62] uses a $4 \times$ dataset, combining the training sets from DIV2K [1] and Flickr2K [52] over 0.5M iterations. Similar as data process in the previous SR3 setting, each image is partitioned into patches of 256x256 pixels to serve as HR ground truths. The LR image patches, resized to 64x64 pixels, are derived by downscaling the HR patches with a bicubic kernel. The VQGAN encoder, pre-trained on the ImageNet dataset, processes these LR patches to distill salient features, furnishing the necessary conditioning input for the following latent denoiser network. For performance evaluation, we use the entire DIV2K validation set, which comprises 100 images. The HR images are downsampled to LR with a bicubic kernel, and then segmented into 64x64 pixel patches, maintaining an 8-pixel overlap between adjacent patches. The latent denoiser model is applied to the LR patches to generate the corresponding SR latent codes. These latent codes are subsequently processed by the VQGAN decoder to reconstruct the SR patches, thereby producing the final high-resolution super-resolution images. The training regimen employs the Adam optimizer with a consistent learning rate of 5×10^{-5} and a batch size of 32 patches. A linear beta scheduler is utilized over 50 steps, selected evenly from a linearly spaced 2000-steps schedule beginning at 10^{-6} and increasing to 10^{-2} . The training is conducted using two 24GB NVIDIA RTX A5000.

7. Additional experimental results

In this section, we begin by providing additional results on the acceleration of training and sampling across various baselines and datasets in Section 7.1. Lastly, in Section 7.2, we offer a more comprehensive visual comparison on the general scene dataset, using the SR3 [44] and ResShift [62] models as baselines.

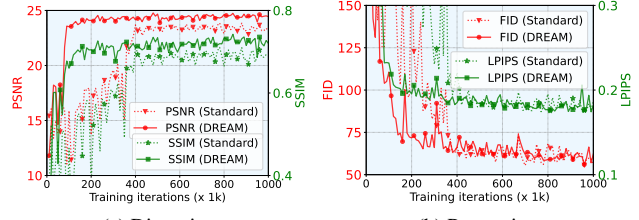


Figure 10. Evolution of distortion metrics (left) and perceptual metrics (right) using SR3 as a baseline on the face dataset.

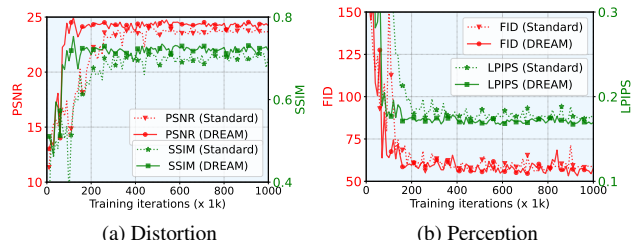


Figure 11. Evolution of distortion metrics (left) and perceptual metrics (right) using IDM as a baseline on the face dataset.

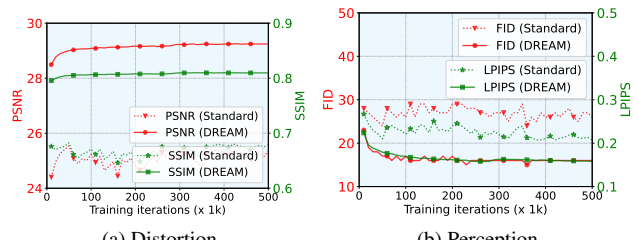


Figure 12. Evolution of distortion metrics (left) and perceptual metrics (right) using ResShift as a baseline on the DIV2K dataset.

7.1. Training and sampling acceleration

Training efficiency. In Table 5, we detail the training time ratio between our DREAM methodology and standard training approaches across a variety of baselines and datasets. Our DREAM method, which includes only a single additional forward computation, results in a marginal increase in training time. However, it offers a considerable advantage by significantly accelerating training convergence. We further illustrate the evolution of training through distortion metrics, namely PSNR and SSIM, as well as perception metrics such as LPIPS and FID. Utilizing SR3 and IDM as baselines for the face dataset, the improvements are evident in Figure 10 and Figure 11. The ResShift model, used as a baseline for the DIV2K dataset, demonstrates similar enhancements in Figure 12. Notably, DREAM not only facilitates quicker convergence but also outperforms the final outcomes of several baselines after they fully converge. For example, with the face dataset, the SR3 model using DREAM achieves a PSNR of 24.49 and an FID of 61.02 in just 490k iterations, whereas the standard diffusion baseline reaches a PSNR of 23.85 and an FID of 61.98 after 880k iterations. This underlines a substantial training speedup by

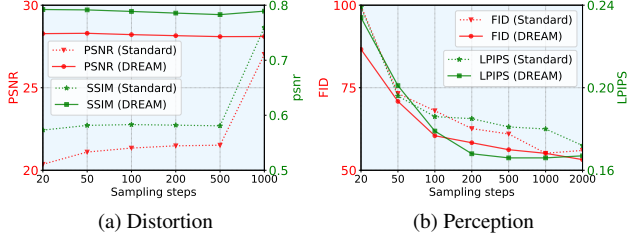


Figure 13. Comparison of distortion metrics (left) and perception metrics (right) with varying sampling steps, using IDM as a baseline on the CelebA-HQ dataset.

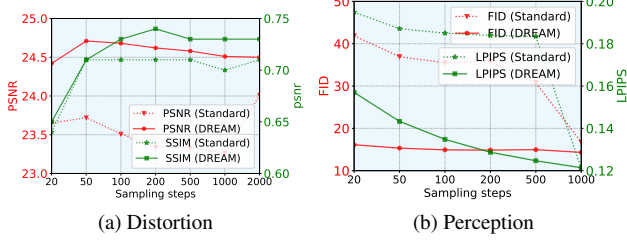


Figure 14. Comparison of distortion metrics (left) and perception metrics (right) with varying sampling steps, using SR3 as a baseline on the DIV2K dataset.

roughly $2\times$ with DREAM. Similarly, the IDM model with DREAM reaches a PSNR of 23.54 and an FID of 55.81 in only 330k iterations, compared to the baseline achieving a PSNR of 23.85 and an FID of 61.98 after 760k iterations, reinforcing the significant efficiency of DREAM.

Sampling acceleration. Furthermore, DREAM significantly enhances the efficiency of the sampling process, surpassing the performance of standard diffusion training with a reduced number of sampling steps. Figure 13 showcases the capabilities of DREAM using the IDM model on the CelebA-HQ dataset. It compares super-resolution images generated with different numbers of sampling steps, evaluating them against both distortion and perception metrics. While the conventional baseline necessitates up to 2000 sampling steps, DREAM attains superior distortion metrics (an SSIM of 0.73 compared to 0.71) and comparable perceptual quality (an LPIPS of 0.179 versus 0.172) with merely 100 steps, leading to an impressive $20\times$ increase in sampling efficiency. In a similar vein, Figure 14a illustrates the impact of DREAM using the SR3 model on the DIV2K dataset. Here, the images produced with varying sampling steps are again evaluated using both sets of metrics. Standard baselines typically require 1000 sampling steps, but with DREAM, improved distortion metrics (an SSIM of 0.79 versus 0.76) and similar perceptual quality (an LPIPS of 0.127 versus 0.121) are achieved with just 100 steps, resulting in a substantial $10\times$ sampling speedup.

7.2. Visualization

Face dataset. In Figure 15 and Figure 16, we provide more representative examples from CelebA-HQ

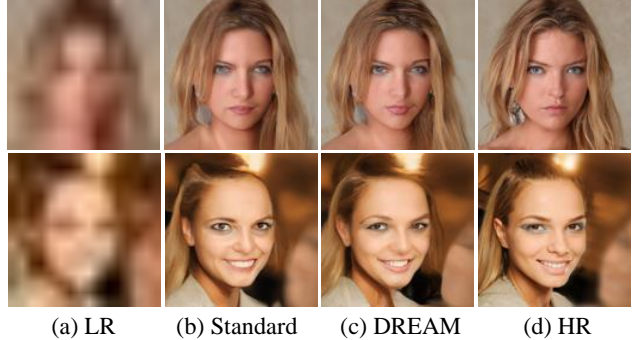


Figure 15. Qualitative comparison for $8\times$ SR using SR3 [44] on the CelebA-HQ dataset [23]. Results highlight DREAM’s superior fidelity and enhanced identity preservation, leading to more realistic details, such as eye and teeth.



Figure 16. Qualitative comparison for $8\times$ SR using IDM [14] on the CelebA-HQ dataset [23]. Results highlight DREAM’s superior fidelity and enhanced identity preservation, leading to more realistic detail generation in features like nose, and wrinkles.

dataset [23], employing SR3 and IDM as baselines, respectively. These results again validate the remarkable ability of DREAM strategy in synthesizing high-fidelity face images.

General scene dataset. To further illustrate the broad effectiveness of our DREAM strategy, we present a selection of examples from the DIV2K [1]. These examples showcase complex image elements such as intricate textures, repeated symbols, and distinct objects. We conduct a comparative visualization of our DREAM strategy against standard training practices, employing the SR3 model as a baseline in Figure 17, Figure 18 and Figure 19. Similarly, we use the ResShift model as a baseline in Figure 20, Figure 21 and Figure 22. The comparisons unequivocally demonstrate the superior performance of our DREAM strategy.

8. Ethic impact

This research is applicable to the task of enhancing human facial resolution, a frequent requirement in mobile photography. It does not inherently contribute to negative social consequences. However, given concerns surrounding personal security, it is crucial to safeguard against its potential misuse for harmful intentions.



(a) Standard



(b) DREAM

Figure 17. Qualitative comparison for 4 \times SR on DIV2K [1] using SR3 [44] model as baseline. **Left Image:** standard training; **Right Image:** DREAM training. The model trained under DREAM framework exhibits enhanced fine-grained details and rendering more realistic results, as indicated by the magnified section of the synthesized SR images.



(a) Standard



(b) DREAM

Figure 18. Qualitative comparison for 4 \times SR on DIV2K [1] using SR3 [44] model as baseline. **Left Image:** standard training; **Right Image:** DREAM training. The model trained under DREAM framework exhibits enhanced fine-grained details and rendering more realistic results, as indicated by the magnified section of the synthesized SR images.



(a) Standard



(b) DREAM

Figure 19. Qualitative comparison for 4 \times SR on DIV2K [1] using SR3 [44] model as baseline. **Left Image:** standard training; **Right Image:** DREAM training. The model trained under DREAM framework exhibits enhanced fine-grained details and rendering more realistic results, as indicated by the magnified section of the synthesized SR images.



(a) Standard



(b) DREAM

Figure 20. Qualitative comparison for 4x SR on DIV2K [1] using ResShift [62] model as baseline. **Left Image:** standard training; **Right Image:** DREAM training. The model trained under DREAM framework exhibits enhanced fine-grained details and rendering more realistic results, as indicated by the magnified section of the synthesized SR images.



(a) Standard



(b) DREAM

Figure 21. Qualitative comparison for 4x SR on DIV2K [1] using ResShift [62] model as baseline. **Left Image:** standard training; **Right Image:** DREAM training. The model trained under DREAM framework exhibits enhanced fine-grained details and rendering more realistic results, as indicated by the magnified section of the synthesized SR images.



(a) Standard



(b) DREAM

Figure 22. Qualitative comparison for 4x SR on DIV2K [1] using ResShift [62] model as baseline. **Left Image:** standard training; **Right Image:** DREAM training. The model trained under DREAM framework exhibits enhanced fine-grained details and rendering more realistic results, as indicated by the magnified section of the synthesized SR images.